Nonlinear Analysis: Hybrid Systems 62 (2026) 101786

Contents lists available at ScienceDirect

Nonlinear Analysis: Hybrid Systems

journal homepage: www.elsevier.com/locate/nahs

Adaptive neuromorphic control of a pendulum for sustained rhythmic swing☆,☆☆

Xinxin Zhang [a,*], Blas M. Vinagre [b], Inés Tejado [b], Rodolphe Sepulchre [c,d]

[a] Dept. Applied Physics and Electronics, Umeå University, Umeå, Sweden
[b] Escuela de Ingenierías Industriales, Universidad de Extremadura, Badajoz, Spain
[c] Dept. Electrical Engineering, KU Leuven, KasteelPark Arenberg 10, Leuven, Belgium
[d] Dept. Engineering, University of Cambridge, Trumpington Street, Cambridge CB2 1PZ, UK

ARTICLE INFO

Keywords:
Neuromorphic control
Half-center oscillator
Adaptive control
Pendulum
Swing

ABSTRACT

This work presents the analysis and design of a neuromorphic control system based on a dual Half-Center Oscillator (HCO) architecture. We first perform a theoretical nullcline analysis to characterize the effects of intrinsic neural parameters (including the time constants, coupling gains, and inputs) on HCO dynamics. Based on this analysis, we then propose a design procedure that integrates the specification of key HCO parameters with adaptive control algorithms for rhythmic oscillation with desired amplitude and frequency regulation. Finally, the proposed HCO control system is validated through case studies on a pendulum through simulations. Results successfully demonstrate the controller's ability to induce and sustain rhythmic swings across a wide frequency range from 1 Hz to 100 Hz and various damping ratios.

1. Introduction

Contemporary engineering landscape demands control systems that prioritize high efficiency, adaptability, and robustness [1]. While digital controllers are effective, their reliance on continuous, clock-driven operations often imposes inherent limitations, such as fixed-rate sampling that can restrict dynamic responsiveness and increase energy consumption [2,3]. Thus, there is a compelling impetus to explore discrete, event-based control strategies to enhance both operational efficiency and performance.

Neuromorphic control emerges as a promising alternative, offering a bio-inspired, event-driven paradigm [4]. The core mechanism, implemented through specialized neuromorphic circuits [5], emulates biological neurons: the control signal is event-based, being triggered when a neuron's membrane potential surpasses a specific threshold. This mechanism enables information to be sparsely encoded and transmitted via discrete voltage spikes [6–8]. Compared to clock-driven frameworks, this architecture provides enhanced event-driven energy efficiency and continuous-time responsiveness [6,8]. First, energy efficiency is achieved through sparse communication; the system transmits control signals when the internal membrane potentials cross defined thresholds, eliminating the computational overhead of fixed-rate digital sampling. Second, despite this discrete output mechanism, the internal neural variables evolve via continuous-time differential equations. This continuous integration allows the controller to react instantaneously to incoming physical plant dynamics, circumventing the artificial discretization delays inherent to digital control

☆ This article is part of a Special issue entitled: 'TC1.3 Discrete-event and hybrid systems(IFAC WC 2026)' published in Nonlinear Analysis: Hybrid Systems.

☆☆ This work was partially funded by the Agencia Estatal de Investigación (Ministerio de Ciencia e Innovación) through project PID2022-141409OB-C22/AEI/10.13039/501100011033/FEDER, UE, and by the European Regional Development Fund (FEDER) under the initiative "A Way to Make Europe.".

* Corresponding author.
E-mail addresses: xinxin.zhang@umu.se (X. Zhang), bvinagre@unex.es (B.M. Vinagre), itejbal@unex.es (I. Tejado), rodolphe.sepulchre@kuleuven.be (R. Sepulchre).

https://doi.org/10.1016/j.nahs.2026.101786
Received 3 November 2025; Received in revised form 1 March 2026; Accepted 4 July 2026
Available online 18 July 2026
1751-570X/© 2026 Published by Elsevier Ltd.

loops. Following initial demonstrations in neuron-based servo controllers [9,10], the field has expanded to address intricate systems, including mechanical systems and multi-robot coordination [8,11,12]. Subsequent advances in control theory, such as mixed-feedback systems and neuromodulation techniques, have further matured these controllers, facilitating the synthesis of robust, adaptive, and complex oscillatory behaviors [4,13–16].

One advantage of neuromorphic control is its ability to generate rhythmic output signals by relying on intrinsic, bio-inspired network dynamics. In contrast to methods requiring explicit, time-indexed reference signals, this neuromorphic framework operates as an autonomous nonlinear dynamical system governed by limit cycle attractors [8]. This architecture confers robustness against external perturbations, naturally returning the disturbed state to the established periodic orbit without continuous error computation or trajectory recalculation. Furthermore, adjusting structural parameters in the neuromorphic control model modulates the oscillation frequency and amplitude. However, despite insightful analytical advances in neuromorphic dynamics—including phase portrait analysis [14], hybrid systems theory for stability proofs [12,17], and describing function analysis for rhythmic systems [18], a detailed analysis and design methodology for tuning these inner dynamics to achieve frequency and magnitude regulation of rhythmic oscillation remains elusive. The current gap lies in the absence of a principled approach for synthesizing controllers that effectively exploit the intricate relationship between network parameters and desired rhythmic dynamics. This impedes the widespread implementation of neuromorphic control for autonomous rhythmic motion generation.

This paper addresses this challenge by introducing novel analysis and design methodologies for neuromorphic control systems that utilize Half-Center Oscillator (HCO) [19] structures to generate rhythmic motions. The HCO comprises two reciprocally inhibited neurons, with individual dynamics governed by Morris–Lecar current balance equations [20]. The main contributions of this work are twofold:

- The development of a nullcline analysis for the neural dynamics within the HCO, accompanied by a systematic configuration protocol for dual-HCO-based neuromorphic control to generate rhythmic motions.
- The effectiveness of the dual-HCO neuromorphic controller was validated in simulation on a pendulum, achieving swinging motion with target magnitude and frequency tracking across the 1 Hz to 100 Hz range and various damping ratios.

This control was achieved by relying on the intrinsic bio-dynamics of the HCO control, eliminating the need for external feedback inputs.

The remainder of this paper is organized as follows. Section 2 introduces the fundamental definitions and background of HCOs. Section 3 details the analysis and design methodology for the HCO-based neuromorphic controller. Sections Section 4 presents and discusses the simulation results, validating the control framework.[1] Finally, Section 5 offers concluding remarks and outlines potential avenues for future research.

2. Preliminaries

2.1. Neuromorphic half-center oscillator dynamics

Neuromorphic control systems capture the intrinsic dynamics of biological Central Pattern Generators (CPGs) to produce rhythmic behaviors [14]. At the cellular level, the biological rhythms originate from the temporal evolution of membrane potentials and the gating dynamics of ion channels. Translating these physiological mechanisms into an equivalent electrical circuit, the HCO serves as a fundamental rhythm-generating motif. The HCO represents a minimal circuit configuration where two neural units alternate their activity phases via continuous reciprocal inhibition, converting non-rhythmic inputs into sustained oscillations. Following the Morris–Lecar current balance framework [20], this mechanism is formulated for two mutually inhibitory neurons, indexed by $i \in \{1,2\}$. The state of each neuron i is defined by a three-dimensional vector $(v_i(t), v_{s,i}(t), v_{us,i}(t))$, governed by the following system of nonlinear differential equations [8,13]:

$$\begin{cases} \dot{v}_i(t) = \frac{1}{\tau_f}\left(-v_i(t) + g_f^- \tanh(v_i(t)) - g_s^+ \tanh(v_{s,i}(t)) + g_s^- \tanh(v_{s,i}(t)+0.9) - g_{us}^+ \tanh(v_{us,i}(t)+0.9) + I_{\text{syn},i}(t) + I_i(t)\right), \\ \dot{v}_{s,i}(t) = \frac{1}{\tau_s}(v_i(t) - v_{s,i}(t)), \\ \dot{v}_{us,i}(t) = \frac{1}{\tau_{us}}(v_i(t) - v_{us,i}(t)), \end{cases} \tag{1}$$

where v_i, $v_{s,i}$, and $v_{us,i}$ represent the fast membrane potential, the slow synaptic state, and the ultra-slow adaptation state, respectively. Other system parameters are defined as follows:

- $\tau_f, \tau_s, \tau_{us} \in \mathbb{R}^+$: time constants for the fast, slow, and ultra-slow dynamics, respectively, satisfying the intrinsic time-scale hierarchy $\tau_f \ll \tau_s \ll \tau_{us}$.
- $g_f^-, g_s^+, g_s^-, g_{us}^+ \in \mathbb{R}^+$: positive conductance gains modulating the influence of the intrinsic neural dynamics components.
- $I_i(t)$: external input current applied to neuron i.
- $I_{\text{syn},i}(t)$: the total synaptic coupling current received by postsynaptic neuron i. This generalized term models both the internal synaptic connections within a single HCO and the inter-network cross-connections between distinct HCOs.

[1] The MATLAB code and figures supporting this study are publicly available at Github.

A schematic of the equivalent circuit for Eq. (1) is provided in Supplementary Fig. S1. Within Eq. (1), the constant +0.9 applied to the arguments of the $\tanh(\cdot)$ function acts as a threshold offset for the slow and ultra-slow state variables, $v_{s,i}$ and $v_{us,i}$. This positive bias induces a horizontal shift in the hyperbolic tangent activation curve, generating a non-zero baseline output even when the respective state variables equal zero. This functional asymmetry shapes the resting potentials and the geometry of the resulting oscillatory limit cycle. The specific offset value of 0.9 is adopted from established neuromorphic models [8]. Fixing this parameter reduces the dimensionality of the system, constraining the parameter search space and facilitating the controller tuning protocol.

2.2. Dual half-center oscillator control architecture

The neuromorphic control framework in this study employs a dual HCO architecture comprising four neurons arranged into two coupled pairs: HCO_1 (neurons $i \in \{1,2\}$, defined by state vectors $(v_1, v_{s,1}, v_{us,1})$ and $(v_2, v_{s,2}, v_{us,2})$) and HCO_2 (neurons $i \in \{3,4\}$, defined by state vectors $(v_3, v_{s,3}, v_{us,3})$ and $(v_4, v_{s,4}, v_{us,4})$). This configuration generates a bipolar control signal via a threshold-based switching mechanism [8]:

$$u(t) = G_{h1} \cdot \mathbb{I}_{\{v_1(t) > v_{\text{thr}}\}} \pm G_{h2} \cdot \mathbb{I}_{\{v_3(t) > v_{\text{thr}}\}}, \tag{2}$$

where $G_{h1}, G_{h2} \in \mathbb{R}^+$ represent the output gains, $v_{\text{thr}} \in \mathbb{R}$ denotes the defined firing threshold, and $\mathbb{I}_{\{\cdot\}}$ is the indicator function, defined as:

$$\mathbb{I}_{\{v_i(t) > v_{\text{thr}}\}} = \begin{cases} 1, & \text{if } v_i(t) > v_{\text{thr}}, \\ 0, & \text{otherwise.} \end{cases} \tag{3}$$

The selection of G_{h1}, G_{h2}, and v_{thr} in (2) is dictated by the system's kinematic requirements. This study establishes a systematic protocol to determine these parameters to achieve the target output $u(t)$, as detailed in Section 3.6.

3. Analysis and design for HCO

This section outlines the analysis and design procedure for the dual-HCO neuromorphic control system. First, Sections 3.1 through 3.3 detail the effects of the time constants $(\tau_f, \tau_s, \tau_{us})$, the conductance gains $(g_f^-, g_s^+, g_s^-, g_{us}^+)$, and the external input $(I_i(t))$ on the oscillatory dynamics in (1). Following this analysis, a design method for rhythmic motion control is proposed in Sections 3.4 through 3.6.

3.1. Analysis of time constants in HCO

The following theorem addresses the effects of the fastest time constant, τ_f, on the HCO system dynamics in (1).

Theorem 1 (*Temporal scaling by τ_f*). *For the HCO dynamics in (1), assuming the ratios τ_f/τ_s and τ_f/τ_{us} are invariant, τ_f operates as a global temporal scaling parameter. Modulating τ_f by a factor $\alpha \in \mathbb{R}^+$ scales the temporal evolution of the system by $1/\alpha$, preserving the geometric structure of all phase-space trajectories.*

Proof. Proof is provided in Appendix A.

Remark 1. Theorem 1 establishes a decoupling between the time scale and the state-space geometry of the limit cycle. In the context of control design, modulating the time constant τ_f enables dynamic frequency adaptation while guaranteeing that the amplitude and phase-normalized characteristics of the applied torque remain invariant.

We now turn to the role of the slow and ultra-slow time constants, τ_s and τ_{us}, described by the following theorem:

Theorem 2 (*Low-pass filter role of τ_s and τ_{us}*). *In (1), assuming zero initial conditions ($v_{s,i}(0) = 0$ and $v_{us,i}(0) = 0$), the state variables $v_{s,i}(t)$ and $v_{us,i}(t)$ implement a first-order low-pass filtering of the membrane potential $v_i(t)$. Let $V_i(s)$, $V_{s,i}(s)$, and $V_{us,i}(s)$ denote the Laplace transforms of the corresponding time-domain state variables. The resulting transfer functions are:*

$$H_s(s) = V_{s,i}(s)/V_i(s) = 1/(\tau_s s + 1), \tag{4}$$

$$H_{us}(s) = V_{us,i}(s)/V_i(s) = 1/(\tau_{us} s + 1), \tag{5}$$

where $s \in \mathbb{C}$ denotes the complex Laplace variable. To characterize the low-pass filtering behavior via the frequency response, s is evaluated along the imaginary axis as $s = j\omega$, with $j = \sqrt{-1}$ and $\omega \in \mathbb{R}^+$ representing the angular frequency.

Proof. Applying the Laplace transform to the governing differential equations of $v_{s,i}$ and $v_{us,i}$ in (1), under the assumption of zero initial conditions, yields transfer functions (4)-(5).

Theorem 2 aligns with the linearized HCO membrane analysis in [14].

Remark 2. Theorem 2 isolates the slow burst envelope from the fast membrane potential. The resulting state integration provides a temporal memory that drives both reciprocal inhibition and autonomous burst termination. Ultimately, this dynamic filtering bridges the temporal gap, translating high-frequency neuronal spiking into the slow-timescale macroscopic phase transitions required for mechanical actuation.

3.2. Analysis of gain parameters in HCO

A nullcline is defined as the locus of points in the phase space where a state variable's derivative vanishes ($\dot{x}_i = 0$) [21]. For the HCO neural dynamics (1), the v_i-nullcline ($\mathcal{N} : \dot{v}_i = 0$) is defined by the algebraic equation $v_i = \mathcal{F}(v_i, v_{s,i}, v_{us,i}; \cdot)$ in the $(v_i, \mathcal{F})$ phase space. The nullcline geometry determines the HCO's characteristic rhythmic behavior, which is realized as a limit cycle. While prior literature [14] established foundational input-output current-voltage (I-V) curve analysis for qualitative insights into excitability and bistability via phase portraits, a systematic parameter selection methodology for practical control applications remains an open challenge. Building upon these insights [14], the subsequent analysis, presented in Propositions 1 through 3, utilizes nullcline geometry to relate how the gain parameters $\{g_f^-, g_s^+, g_s^-, g_{us}^+\}$ and external input $I_i(t)$ in (1) affect the system's bifurcation structure. This method isolates the dynamic influence of specific parameters through a decoupled analysis, evaluating individual gains while fixing the remaining system variables to constant baseline values. This analysis yields the design algorithm (Section 3.6) for designing control laws.

Propositions 1 (*Bifurcation and stability from self excitation gain, g_f^-*). *Consider the fast subsystem of the HCO model (1), defined by $\dot{v}_i = \tau_f^{-1}(-v_i + g_f^- \tanh(v_i) + C)$, where C is a constant term encapsulating the aggregate influence of the slow dynamics and external inputs. The self-excitation gain g_f^- serves as the primary bifurcation parameter determining the system's stability regimes:*

(1) Monostable regime ($g_f^- \leq 1$): a unique, globally stable fixed point exists for all $C \in \mathbb{R}$.

(2) Bistable regime ($g_f^- > 1$): the emergence of bistability is contingent upon the magnitude of C. Let v_i^{crit} denote the critical membrane potential satisfying the saddle-node bifurcation condition $g_f^- \operatorname{sech}^2(v_i^{\text{crit}}) = 1$. This critical potential defines the bistable boundary as $C_{\text{crit}}(g_f^-) = |v_i^{\text{crit}} - g_f^- \tanh(v_i^{\text{crit}})|$. The system exhibits bistability (characterized by three fixed points: two stable, one unstable) if and only if the constant bias satisfies $|C| < C_{\text{crit}}(g_f^-)$. Otherwise, a single stable fixed point exists.

Proof. Proof is provided in Appendix B.

Remark 3. Proposition 1 establishes the condition for the fast subsystem to function as a bistable switch. Setting the self-excitation gain $g_f^- > 1$ generates distinct active and quiescent states. This bistable structure provides the mechanism for rhythmic bursting.

Supplementary Fig. S2 provides a visualization of the nullcline analysis from Proposition 1 across three self-excitation gain regimes: $g_f^- < 1$, $g_f^- = 1$, and $g_f^- > 1$.

Propositions 2 (*Role of synaptic gains, g_s^+, g_s^-, and g_{us}^+*). *The synaptic gains $\{g_s^+, g_s^-, g_{us}^+\}$ in the HCO system (1) modulate the system dynamics by inducing vertical translations of the v_i-nullcline ($\mathcal{N} : \dot{v}_i = 0$). The direction and nature of the nullcline translation are determined by the partial derivatives of the modulating term Φ given by*

$$\Phi = -g_s^+ \tanh(v_{s,i}) + g_s^- \tanh(v_{s,i} + 0.9) - g_{us}^+ \tanh(v_{us,i} + 0.9) \tag{6}$$

with respect to the respective gains:

(1) Slow inhibitory gain (g_s^+): increases in g_s^+ cause a downward translation of $\mathcal{N}$ ($\partial\Phi/\partial g_s^+ \leq 0$), promoting lower-voltage quiescent states (inhibition).

(2) Slow excitatory gain (g_s^-): increases in g_s^- cause an upward translation of $\mathcal{N}$ ($\partial\Phi/\partial g_s^- > 0$), promoting higher-voltage active states (excitation).

(3) Ultra-slow adaptive gain (g_{us}^+): increases in g_{us}^+ contribute to a negative shift ($\partial\Phi/\partial g_{us}^+ < 0$). This provides a slow, progressive downward translation of $\mathcal{N}$ as $v_{us,i}(t)$ accumulates, serving as the essential mechanism for burst termination and adaptation.

Proof. Proof is provided in Appendix C.

Remark 4. From a control perspective, the synaptic gains in Proposition 2 dictate the duty cycle and switching thresholds of the oscillator. The static gains, g_s^+ and g_s^-, establish the baseline voltage boundaries for the active and quiescent states. The adaptive gain, g_{us}^+, functions as an internal state timer; its accumulation shifts the nullcline until a phase transition is forced. This dynamic geometric modulation generates autonomous rhythmic bursting independent of external clock signals.

Supplementary Fig. S3 illustrates the nullcline analysis corresponding to Proposition 2, detailing how the modulation of the inhibitory (g_s^+), excitatory (g_s^-), and ultra-slow adaptive (g_{us}^+) synaptic gains geometrically influences the system's fixed points.

3.3. Bifurcation control via external input current $I_i(t)$

Propositions 3 (*Bifurcation control via external input current, $I_i(t)$*). *The external input current $I_i(t)$ functions as a bifurcation control parameter by inducing a direct vertical translation of the v_i-nullcline ($\mathcal{N} : \dot{v}_i = 0$). For a system operating in the bistable configuration ($g_f^- > 1$), a positive $I_i(t)$ eliminates the low-voltage stable fixed point, thereby enforcing a transition to the high-voltage active regime.*

Proof. Proof is provided in Appendix D.

Supplementary Fig. S4 shows how the $I_i(t)$ induces state switching via vertical nullcline translation.

Remark 5. In a control context, the external current $I_i(t)$ serves as a triggering mechanism. By collapsing the bistable hysteresis loop, an applied input forcefully overrides the intrinsic oscillation cycle, driving an immediate state transition. This property allows the neuromorphic controller to integrate sensory feedback or higher-level supervisory commands, synchronizing the endogenous rhythm with external mechanical events.

3.4. Synaptic current $I_{syn,i}(t)$ formulation

The synaptic current $I_{\text{syn},i}(t)$ encapsulates the network coupling from surrounding units to the postsynaptic neuron i [5]. The synaptic transmission from a presynaptic neuron j to neuron i is formulated using either a logistic sigmoid function:

$$I_{\text{syn},i}(t) = g_{\text{s},ij} \cdot (1 + \exp(-\alpha_{1,ij}(v_{s,j}(t) + \alpha_{2,ij})))^{-1}, \tag{7}$$

or a hyperbolic tangent function:

$$I_{\text{syn},i}(t) = g_{\text{t},ij} \cdot \tanh\big(\beta_{1,ij} v_{s,j}(t) + \beta_{2,ij}\big), \tag{8}$$

where the parameters $\{g_{s,ij}, \alpha_{1,ij}, \alpha_{2,ij}, g_{t,ij}, \beta_{1,ij}, \beta_{2,ij}\} \in \mathbb{R}$ define the coupling strength, transition sharpness, and horizontal shift. The key functional difference lies in the output range: the sigmoid in (7) maps to $(0, 1)$, while the tanh in (8) maps to $(-1, 1)$.

Within a single HCO, synaptic inhibition is symmetric and typically achieved by setting $g_{s,ij} < 0$ in the sigmoid formulation. When generalizing to the dual HCO configuration, $I_{\text{syn},i}(t)$ incorporates both this symmetric intra-HCO mutual inhibition and additional inter-HCO cross-connections. These cross-connections are configured as asymmetric inputs to enable the coordinated interaction between the different HCO components.

3.5. Control signal $u(t)$ design

Diverging from the discrete, threshold-based pulse outputs defined in (2), this formulation generates the control signal $u(t)$ using a continuous sigmoidal activation function. This smooth transition prevents abrupt actuator switching, thereby mitigating high-frequency chattering and reducing mechanical wear on the physical plant. The resulting control input is derived from the membrane potentials of the primary neurons, v_1 and v_3, across the two respective HCOs:

$$u(t) = G_{h1} \cdot \sigma(v_1(t), v_{\text{thr}}) - G_{h2} \cdot \sigma(v_3(t), v_{\text{thr}}), \tag{9}$$

where the sigmoidal function σ is defined as:

$$\sigma(v, v_{\text{thr}}) = (1 + \exp(-2(v - v_{\text{thr}})))^{-1}, \tag{10}$$

with $G_{h1}, G_{h2} \in \mathbb{R}^+$ representing the torque gains, and $v_{\text{thr}} \in \mathbb{R}$ being the activation threshold.

3.6. Adaptive neuromorphic controller design protocol

Building upon the established theoretical framework (Sections Section 3.1–3.5), this section outlines the parameter configuration protocol for the dual-HCO neuromorphic controller. The primary control objective is to tune the parameters of (1) to shape the intrinsic dynamics of the single HCO. Once configured, these units are integrated into the dual-HCO architecture to generate a control input that drives the physical plant at a target amplitude ($A_{\text{real}} \in \mathbb{R}^+$) and reference frequency ($\omega_{\text{ref}} \in \mathbb{R}^+$).

Achieving the tracking objective relies on configuring three characteristics of the control input signal $u(t)$ generated by the dual-HCO controller: frequency, duration, and magnitude. This configuration follows a four-step procedure: (i) regime calibration, which adjusts intrinsic gains (e.g., g_f^-) to establish the target active bursting dynamics; (ii) frequency alignment, which allows to modulate the fast time constant τ_f to synchronize the output pulse frequency with the reference frequency, ω_{ref}; (iii) duration modulation, which sets the output threshold v_{thr} to determine the pulse width of the control signal; and (iv) magnitude adaptation, which implements an adaptive mechanism to scale the control pulse amplitude, defining the required energy injection for the plant.

The detailed tuning procedure is summarized as follows:

(1) Gain parameter establishment: in accordance with Propositions 1 and 2, configure the synaptic gains (g_f^-, g_s^+, g_s^-, g_{us}^+) to modify the nullcline geometry, thereby establishing the required excitatory and bistable operational regimes.

(2) Input current configuration: the external input $I_i(t)$ is configured based on the demands of the overall feedback loop. For the inter-neuron synaptic input $I_{\text{syn},i}(t)$, Eq. (7) or (8) is employed to model the coupling dynamics.

(3) Time constant setting: the intrinsic time-scale hierarchy, $\tau_f < \tau_s < \tau_{us}$, is maintained. By fixing the ratios τ_f/τ_s and τ_f/τ_{us}, the absolute value of the fast time constant τ_f is adjusted (per Theorem 1) to linearly align the system's intrinsic oscillation frequency with the target reference frequency, ω_{ref}.

(4) Output threshold determination: the initial output threshold v_{thr} in (9) is set at the midpoint of the membrane voltage's operating range: $v_{\text{thr}} = (\max(v_1(t)) + \min(v_1(t)))/2$. Then, fine-tuning v_{thr} allows for adjustment of the controller's output pulse width.

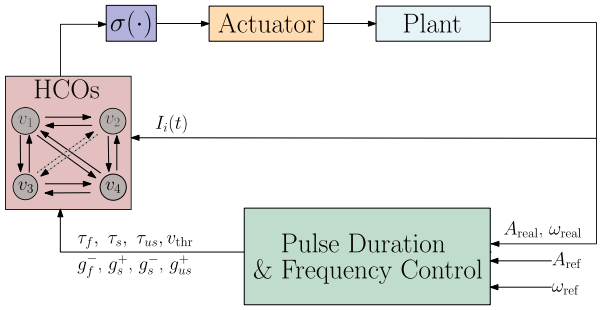


Fig. 1. Block diagram of the dual-HCO neuromorphic control system, adapted from [8].

(5) Adaptive output gain control: an adaptive mechanism dynamically adjusts the control output gains, G_{h1} and G_{h2}, in (9) to minimize the amplitude tracking error, $\Delta A = A_{\text{ref}} - A_{\text{real}}$. For symmetric oscillatory trajectories, these gains are constrained such that $G_{h1}(t) = G_{h2}(t)$. They are updated via a discrete adaptive law executed once per oscillation period, $\Delta t = 1/f_\theta$, where f_θ is the target frequency:

$$G_{h1}(t) = G_{h1}(t - \Delta t) + \eta \tanh(\Delta A). \tag{11}$$

The tangent function bounds the magnitude of the update step, facilitating smooth convergence. Defining the learning rate as $\eta = f_\theta$ scales the adaptation proportionally with the target frequency, compensating for increased inertial demands at higher velocities. Furthermore, alternative adaptive update laws can be implemented depending on the specific operational requirements of the system. While (11) assumes a balanced oscillation, the architecture can accommodate asymmetric tasks. Assigning independent values ($G_{h1} \neq G_{h2}$) generates an asymmetric control output $u(t)$, shifting the center of the oscillatory orbit. This directional bias in the limit cycle enables the controller to execute unidirectional locomotion or reject constant asymmetric disturbances. In such cases, independent adaptive laws govern $G_{h1}(t)$ and $G_{h2}(t)$ to track distinct clockwise and counterclockwise reference amplitudes.

Finally, the overall control architecture is depicted in Fig. 1, which drives the system dynamics with rhythmic motions. The following section illustrates the systematic, step-by-step design process through a case study.

4. Case study: Rhythmic pendulum control using dual-HCO networks

4.1. Pendulum system dynamics

This study applies a rigid-body pendulum as the benchmark for rhythmic neuromorphic control, defined by

$$J \cdot \ddot{\theta}(t) + b \cdot \dot{\theta}(t) + mgL/2 \cdot \sin\theta(t) = \tau(t), \tag{12}$$

where $\theta(t)$ is the angular displacement and $\tau(t)$ is the applied torque. The physical parameters are: length $L = 0.36$ m, density $\rho = 1000$ kg/m^3, radius $r = 0.02$ m, and viscous damping $b = 1$ N $\cdot$ m $\cdot$ s/rad. The mass and moment of inertia are $m \approx 0.4524$ kg and $J \approx 0.0196$ kg $\cdot$ m^2.

4.2. Dual-HCO neuromorphic controller design

The controller employs a dual HCO architecture consisting of four neurons ($i \in \{1, 2, 3, 4\}$) governed by the dynamics defined in (1). The control objective is to induce pendulum oscillations with a target amplitude of $A = 1$ rad and frequency $f_\theta \in \mathbb{R}^+$. The design adheres to the systematic protocol outlined in Section 3.6:

(1) Gain parameters. The intrinsic neural dynamics are configured for a bistable regime with $g_f^- = 2$, $g_s^+ = 1$, $g_s^- = 1.5$, and $g_{us}^- = 1.5$.

(2) Input current configuration. In this case study, we rely on the intrinsic dynamics of the HCO system to generate oscillations. Thus, the external input is fixed at a constant bias of $I_i = -1.0$. However, as demonstrated in the case study in Supplementary Material, I_i can alternatively be formulated as a closed-loop sensory feedback signal, enabling the oscillator to entrain to the natural resonance of the mechanical plant. The total synaptic input $I_{\text{syn},i}(t)$ incorporates both mutual inhibition within each HCO and cross-inhibition between HCOs:

$$\begin{aligned}
I_{\text{syn},1}(t) &= \sigma_\gamma(v_{s,2}, -0.2) - 1.5\tanh(v_3),\\
I_{\text{syn},2}(t) &= \sigma_\gamma(v_{s,1}, -0.2) + 1.5\tanh(v_3),\\
I_{\text{syn},3}(t) &= \sigma_\gamma(v_{s,4}, -0.2) - 1.5\tanh(v_1),\\
I_{\text{syn},4}(t) &= \sigma_\gamma(v_{s,3}, -0.2) + 1.5\tanh(v_1),
\end{aligned} \tag{13}$$

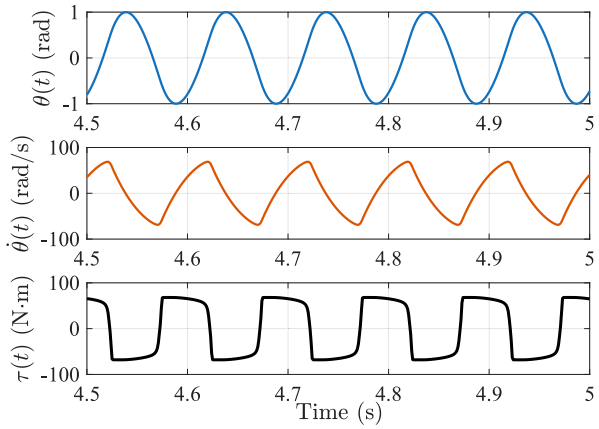


Fig. 2. Time-domain steady-state response of the pendulum under neuromorphic control. (Top) Pendulum angle $\theta(t)$, (middle) angular velocity $\dot{\theta}(t)$, and (bottom) control torque $\tau(t)$ over 0.5 s of simulation.

where the sigmoidal synaptic transfer function is $\sigma_\gamma(v,\gamma) = \gamma/(1+\exp(-2(v+1)))$. In (13), the constant -0.2 serves as the intra-network mutual inhibition weight (γ). Acting through the sigmoidal synaptic transfer function σ_γ, this parameter enforces reciprocal inhibition, causing the two constituent neurons of a single HCO (e.g., v_1 and v_2) to oscillate in an anti-phase relationship (i.e., in opposite directions). This mechanism establishes the baseline rhythmic oscillation within each isolated HCO. Conversely, the constant 1.5 denotes the inter-network cross-coupling strength, which governs the phase synchronization dynamics between the two distinct HCOs. In practical control designs, this cross-coupling constant can be tuned based on the desired synchronization speed and the requirement for robustness against external perturbations.

(3) Time constants and frequency scaling. The baseline time constants for $f_{\text{base}} = 1$ Hz are $\tau_{f,\text{base}} = 0.01005$ s, $\tau_{s,\text{base}} = 20\tau_{f,\text{base}}$ s, and $\tau_{us,\text{base}} = 100\tau_{f,\text{base}}$ s. To align the controller's rhythm with the desired frequency f_θ, all time constants are scaled according to Theorem 1:

$$\tau_k = \tau_{k,\text{base}} \cdot (f_{\text{base}}/f_\theta), \quad k \in \{f, s, us\}. \tag{14}$$

(4) The output threshold is fixed at $v_{\text{thr}} = 0$.

(5) Adaptive gain mechanism. The output torque gains $G_{h1}(t) = G_{h2}(t)$ apply the adaptive law in (11).

4.3. Simulation results

Fig. 2 demonstrates the system's steady-state performance, achieving successful tracking of swing motions with the target frequency $f_\theta = 10$ Hz and amplitude $A = 1$ rad. The underlying neural dynamics are detailed in Fig. 3. The membrane potentials exhibit stable limit-cycle oscillations with an anti-phase relationship within each HCO (v_1 and v_2; v_3 and v_4) and a quadrature phase coupling between the two HCOs.

4.3.1. Gain adaptation with varying frequency and damping

The frequency adaptability and parametric scalability of the proposed architecture are evaluated by sweeping the operating frequency across a logarithmic range of 50 points (1–100 Hz) under varying damping conditions ($b \in \{0.5, 1.0, 2.0\}$ N·m·s/rad). Fig. 4 presents the required terminal steady-state torque gains. The designation "terminal" refers to the converged value attained by the adaptive mechanism defined in (11). This mechanism updates the gain once per period to track the target amplitude, ultimately converging to the terminal gain required to sustain the steady-state oscillation. Two primary scaling relationships are observed: (i) the required torque gain increases monotonically with the oscillation frequency to counteract elevated inertial forces at higher rates, and (ii) for a fixed frequency, higher damping coefficients necessitate an increase in torque gain to overcome enhanced energy dissipation.

4.3.2. Threshold-dependent pulse shaping

Furthermore, adjusting the output threshold v_{thr} provides a direct mechanism for shaping the smoothed pulse duration, allowing the control signal to be tailored to specific actuator constraints or energy optimization objectives.

Fig. 5 illustrates the effects of the output threshold v_{thr} on the steady-state torque gains across the frequency sweep for a damping coefficient of $b = 1$ N·m·s/rad. Compared to $v_{\text{thr}} = 0$, the case with $v_{\text{thr}} = 3$ results in a narrower, more impulsive control signal. Therefore, the adaptive gain mechanism compensates for this reduced pulse width. Specifically, to maintain the target oscillation amplitude, the mechanism necessitates and implements a higher torque magnitude.

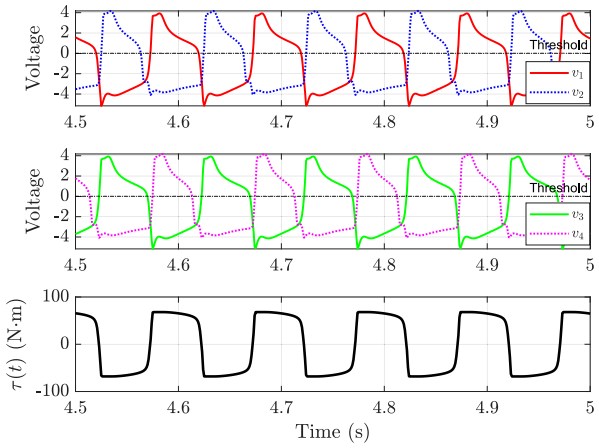


Fig. 3. (Top) Voltages of neurons v_1 and v_2 in HCO_1, (middle) voltages of neurons v_3 and v_4 in HCO_2, and (bottom) torque $\tau(t)$ over 0.5 s of simulation.

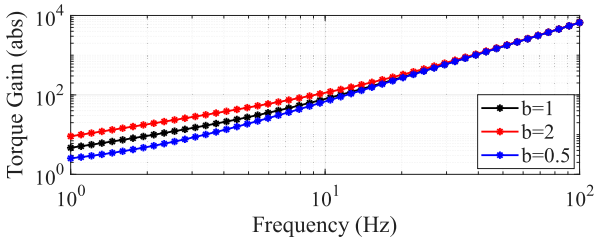


Fig. 4. Terminal torque (output) gains of the neuromorphic controller, $G_{h1}(t_{\text{terminal}}) = G_{h2}(t_{\text{terminal}})$, obtained over a 1–100 Hz frequency sweep for damping coefficients $b = 0.5$, $b = 1$, and $b = 2$.

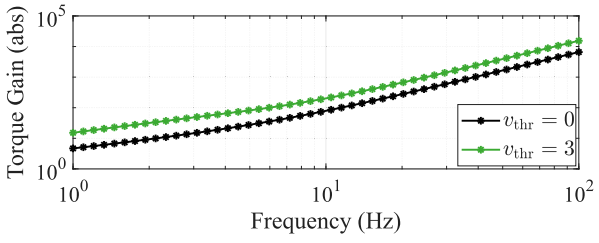


Fig. 5. Terminal torque gains of the dual-HCO controller, $G_{h1}(t_{\text{terminal}}) = G_{h2}(t_{\text{terminal}})$, obtained over a 1–100 Hz frequency sweep for $v_{\text{thr}} = 0$ and $v_{\text{thr}} = 3$.

5. Conclusion

This work introduces a neuromorphic control framework predicated on a dual HCO architecture. The study first provides a nullcline analysis of the neural dynamics within the HCO model, accompanied by a design protocol for the dual-HCO control system. The proposed framework is then validated through simulations executing the rhythmic control of a pendulum. By calibrating the system parameters—specifically, the time constants, synaptic gains, input currents, and adaptive output gains—the dual-HCO controller drives oscillatory motion across a target frequency range of 1 Hz to 100 Hz under varying damping conditions ($b \in \{0.5, 1, 2\}$). Additionally, this approach circumvents the reliance on external reference signals and explicit trajectory generation. The application of this control methodology to inverted pendulum stabilization was also investigated and will be detailed in subsequent research.

Moreover, from the nullcline analysis in Section 3.3, utilizing the external input $I_i(t)$ to integrate sensory feedback enables the architecture to achieve energy-efficient, plant-driven phase synchronization, a case study for which is provided in the Supplementary Material.

Two primary objectives warrant future investigation: (i) implementation on a physical neuromorphic hardware platform to evaluate energy efficiency and operational performance, and (ii) the development of advanced adaptive learning mechanisms to autonomously compensate for unmodeled dynamics and external disturbances.

CRediT authorship contribution statement

Xinxin Zhang: Writing – review & editing, Writing – original draft, Visualization, Validation, Software, Project administration, Methodology, Investigation, Formal analysis, Data curation, Conceptualization. **Blas M. Vinagre:** Conceptualization, Funding acquisition, Investigation, Methodology, Project administration, Resources, Software, Supervision, Validation, Writing – review & editing. **Inés Tejado:** Writing – review & editing, Supervision, Methodology, Investigation, Funding acquisition, Conceptualization. **Rodolphe Sepulchre:** Writing – review & editing, Supervision, Methodology, Investigation, Conceptualization.

Declaration of competing interest

The authors declare that they have no known competing financial interests or personal relationships that could have appeared to influence the work reported in this paper.

Appendix A. Proof of Theorem 1

Proof. To demonstrate the temporal scaling property, we introduce the non-dimensional time variable $\tilde{t} = t/\tau_f$. By the chain rule, the time derivative transforms as $\frac{d}{dt} = \frac{d\tilde{t}}{dt}\frac{d}{d\tilde{t}} = \frac{1}{\tau_f}\frac{d}{d\tilde{t}}$. Substituting this transformation into (1) yields the rescaled dynamics, given by

$$\begin{aligned}
\frac{dv_i}{d\tilde{t}} &= -v_i + g_f^- \tanh(v_i) - g_s^+ \tanh(v_{s,i}) + g_s^- \tanh(v_{s,i} + 0.9) - g_{us}^+ \tanh(v_{us,i} + 0.9) + I_{\mathrm{syn},i}(\tilde{t}) + I_i(\tilde{t}),\\
\frac{dv_{s,i}}{d\tilde{t}} &= k_s(v_i - v_{s,i}),\\
\frac{dv_{us,i}}{d\tilde{t}} &= k_{us}(v_i - v_{us,i}),
\end{aligned}$$

where $k_s = \tau_f/\tau_s$ and $k_{us} = \tau_f/\tau_{us}$.

Defining the state vector $\mathbf{v} = [v_i, v_{s,i}, v_{us,i}]^T$, the non-dimensional system is:

$$\frac{d\mathbf{v}}{d\tilde{t}} = \mathbf{G}(\mathbf{v}, k_s, k_{us}, \text{gains}, I_i(\tilde{t}), I_{\mathrm{syn},i}(\tilde{t})). \tag{A.1}$$

Since the time constant ratios k_s and k_{us} are held constant, the vector field $\mathbf{G}$ is independent of the absolute value of τ_f. Consequently, the geometric structure of all trajectories in the phase space defined by $\frac{d\mathbf{v}}{d\tilde{t}}$ is invariant under changes to τ_f.

The physical time t is recovered via $t = \tau_f\tilde{t}$. If τ_f is scaled by a factor α, such that $\tau_f' = \alpha\tau_f$, the time required to traverse the invariant non-dimensional trajectory $\tilde{T}$ is $T' = \tau_f'\tilde{T} = \alpha\tau_f\tilde{T} = \alpha T$. Thus, the period T scales linearly with τ_f. This concludes the proof.

Appendix B. Proof of Proposition 1

Proof. The proof proceeds via a fast-slow decomposition and fixed-point analysis of the one-dimensional fast subsystem through 3 steps.

Step 1. Fixed Point and Nullcline Analysis

By treating the slow state variables and external inputs as a constant parameter $C \in \mathbb{R}$, the fixed points, v_i^*, are determined by setting $\dot{v}_i = 0$, yielding the algebraic equation:

$$v_i^* = g_f^- \tanh(v_i^*) + C. \tag{B.1}$$

The number of fixed points corresponds to the number of intersections between the identity line $y_1 = v_i$ and the fast nullcline $y_2 = g_f^- \tanh(v_i) + C$. C acts as a vertical translation of y_2, while the maximum slope of y_2 is governed solely by g_f^-, specifically $\max\left(\frac{\partial y_2}{\partial v_i}\right) = g_f^-$.

Step 2. Stability and Bifurcation Condition

The local stability of a fixed point v_i^* is determined by the sign of the Jacobian, $J = \partial\dot{v}_i/\partial v_i$, evaluated at v_i^*:

$$J = \left(-1 + g_f^- \mathrm{sech}^2(v_i^*)\right)/\tau_f. \tag{B.2}$$

A fixed point is stable if $J < 0$ and unstable if $J > 0$. A saddle–node bifurcation occurs when the fixed point becomes marginally stable ($J = 0$), which requires the critical potential v_i^{crit} to satisfy the condition:

$$g_f^- \operatorname{sech}^2(v_i^{\text{crit}}) = 1. \tag{B.3}$$

Step 3. Bifurcation Analysis by Case

The potential for multi-stability hinges on whether the maximum slope of the fast nullcline exceeds the slope of the identity line, i.e., whether $g_f^- > 1$. We have two cases:

(1) Case $g_f^- \le 1$ (monostable regime): since $g_f^- \le 1$ and $\operatorname{sech}^2(v_i^*) \le 1$, it follows that $g_f^- \operatorname{sech}^2(v_i^*) < 1$ for all $v_i^* \in \mathbb{R}$, which implies $J < 0$. Therefore, any fixed point must be stable. Geometrically, the maximum slope of y_2 is less than or equal to 1, guaranteeing a single intersection with y_1 for all $C \in \mathbb{R}$. The system is globally monostable.

(2) Case $g_f^- > 1$ (bistable regime): the maximum slope of y_2 is $g_f^- > 1$. This allows for three intersections with the identity line y_1 when the vertical shift C is sufficiently small. These three fixed points consist of two stable nodes ($J < 0$) separated by one central unstable saddle ($J > 0$). The boundaries of this bistable region are defined by the saddle–node bifurcation, where two fixed points merge and vanish. This occurs when the fixed point condition (B.1) and the marginal stability condition (B.3) are simultaneously satisfied for the critical values $(v_i^{\text{crit}}, C_{\text{crit}})$. From (B.3), the critical potential is:

$$v_i^{\text{crit}} = \operatorname{arsech}\left(1/\sqrt{g_f^-}\right). \tag{B.4}$$

Substituting (B.4) into (B.1), we have

$$C_{\text{crit}}(g_f^-) = \left| v_i^{\text{crit}} - g_f^- \tanh(v_i^{\text{crit}}) \right|. \tag{B.5}$$

Bistability is possible if and only if $g_f^- > 1$ and $|C| < C_{\text{crit}}(g_f^-)$. If $|C| \ge C_{\text{crit}}(g_f^-)$, the nullcline is shifted such that only one stable fixed point remains. The critical gain $g_f^- = 1$ marks the pitchfork bifurcation point for the emergence of the bistable regime. This concludes the proof.

Appendix C. Proof of Proposition 2

Proof. From (1), The v_i-nullcline defined by the condition $\dot{v}_i = 0$ is given by

$$v_i = g_f^- \tanh(v_i) + \Phi + I_{\text{ext}} = \mathcal{F}(v_i, v_{s,i}, v_{us,i}; \cdot),$$

where $I_{\text{ext}} = I_{\text{syn},i} + I_i$, and Φ encapsulates all slow-variable contributions as defined in (6). Because the term $g_f^- \tanh(v_i)$ operates independently of the synaptic gains, the translation of the nullcline $\mathcal{N}$ along the $\mathcal{F}$-axis is governed by the partial derivatives of the modulating term Φ. The specific effects of varying each respective gain are as follows:

(1) Slow inhibitory gain (g_s^+): the derivative is $\frac{\partial \Phi}{\partial g_s^+} = -\tanh(v_{s,i})$. For active states where $v_{s,i} \ge 0$, we have $\tanh(v_{s,i}) \ge 0$, which ensures $\frac{\partial \Phi}{\partial g_s^+} \le 0$. Thus, an increase in g_s^+ induces a negative (downward) translation of $\mathcal{N}$, promoting inhibition.

(2) Slow excitatory gain (g_s^-): the derivative is $\frac{\partial \Phi}{\partial g_s^-} = \tanh(v_{s,i} + 0.9)$. The positive offset 0.9 ensures that $\tanh(v_{s,i} + 0.9) > 0$ for all physiologically relevant $v_{s,i}$. Hence, $\frac{\partial \Phi}{\partial g_s^-} > 0$. An increase in g_s^- produces a positive (upward) translation, promoting excitation.

(3) Ultra-slow adaptive gain (g_{us}^+): the derivative is $\frac{\partial \Phi}{\partial g_{us}^+} = -\tanh(v_{us,i} + 0.9)$. Since $\tanh(v_{us,i} + 0.9) > 0$, we have $\frac{\partial \Phi}{\partial g_{us}^+} < 0$. Increases in g_{us}^+ induce a negative (downward) nullcline shift.

Appendix D. Proof of Proposition 3

Proof. The v_i-nullcline is determined by the condition $\dot{v}_i = 0$, which yields the explicit relationship:

$$v_i = g_f^- \tanh(v_i) + \Phi(\mathbf{v}_{\text{slow}}) + I_i(t), \tag{D.1}$$

where $\Phi(\mathbf{v}_{\text{slow}})$ represents the constant contribution of the slow variables (as defined in Proposition 2), and $\mathbf{v}_{\text{slow}} = (v_{s,i}, v_{us,i})$. The fixed points occur at the intersections of the nullcline (D.1) and the identity line, $y = v_i$.

Since the external input $I_i(t)$ is an additive term independent of the state variables $\mathbf{v}$, any change in $I_i(t)$ results in a pure vertical translation of the entire nullcline within the phase portrait. This translation directly modulates the overall constant bias $C = \Phi(\mathbf{v}_{\text{slow}}) + I_i(t)$.

As $I_i(t)$ increases, the resultant upward translation of the nullcline forces the low-voltage stable and central unstable fixed points to merge. Once $I_i(t)$ exceeds a critical value, these two fixed points annihilate via a saddle–node bifurcation on a fold. This event removes the stable attractor associated with the silent regime. Thus, the system is left with only the single stable fixed point located on the upper branch of the nullcline, forcing the trajectory to transition abruptly and irreversibly to the high-voltage active state.

Appendix E. Supplementary data

Supplementary material related to this article can be found online at https://doi.org/10.1016/j.nahs.2026.101786.

Data availability

Data will be made available on request.

References

[1] Graham Clifford Goodwin, Stefan F Graebe, Mario E Salgado, et al., Control system design, vol. 240, Prentice Hall Upper Saddle River, 2001.
[2] Rolf Isermann, Digital Control Systems, Springer Science & Business Media, 2013.
[3] Katsuhiko Ogata, Discrete-Time Control Systems, Prentice-Hall, Inc., 1995.
[4] Rodolphe Sepulchre, Timothy O'Leary, Guillaume Drion, Alessio Franci, Control by neuromodulation: A tutorial, in: 2019 18th European Control Conference, ECC, IEEE, 2019, pp. 483–497.
[5] Luka Ribar, Synthesis of neuromorphic circuits with neuromodulatory properties (Ph.D. thesis), 2020.
[6] Rodolphe Sepulchre, Spiking control systems, Proc. IEEE 110 (5) (2022) 577–589.
[7] Christian Fernandez Lorden, et al., Neuromorphic control of embodied central pattern generators, 2023.
[8] Raphael Schmetterling, Fulvio Forni, Alessio Franci, Rodolphe Sepulchre, Neuromorphic control of a pendulum, IEEE Control. Syst. Lett. 8 (2024) 1235–1240.
[9] Steve De Weerth, Lars Nielsen, Carver Mead, Karl Astrom, A neuron-based pulse servo for motion control, in: Proceedings., IEEE International Conference on Robotics and Automation, IEEE, 1990, pp. 1698–1703.
[10] Stephen P. DeWeerth, Lars Nielsen, Carver A. Mead, Karl Johan Åström, A simple neuron servo, IEEE Trans. Neural Netw. 2 (2) (1991) 248–251.
[11] Charlotte Cathcart, Ian Xul Belaustegui, Alessio Franci, Naomi Ehrich Leonard, Spiking nonlinear opinion dynamics (s-NOD) for agile decision-making, IEEE Control. Syst. Lett. (2024).
[12] Elena Petri, Romain Postoyan, WPMH Heemels, Rhythmic neuromorphic control of a pendulum: A hybrid systems analysis, in: 2025 IEEE 64th CDC, IEEE, 2025, pp. 19–24.
[13] Luka Ribar, Rodolphe Sepulchre, Neuromodulation of neuromorphic circuits, IEEE Trans. Circuits Syst. I. Regul. Pap. 66 (8) (2019) 3028–3040.
[14] Luka Ribar, Rodolphe Sepulchre, Neuromorphic control: Designing multiscale mixed-feedback systems, IEEE Control Syst. Mag. 41 (6) (2021) 34–63.
[15] Weiming Che, Fulvio Forni, Dominant mixed feedback design for stable oscillations, IEEE Trans. Autom. Control 69 (2) (2023) 1133–1140.
[16] Omar Juarez-Alvarez, Alessio Franci, Collective rhythm design in coupled mixed-feedback systems through dominance and bifurcations, IEEE Trans. Control. Netw. Syst. (2025).
[17] Elena Petri, Koen J.A. Scheres, E. Steur, WPMH Heemels, Analysis of a simple neuromorphic controller for linear systems: A hybrid systems perspective, in: 2024 IEEE 63rd CDC, IEEE, 2024, pp. 8578–8583.
[18] Taisia Medvedeva, Fernando Castaños, Alessio Franci, Formalizing neuromorphic control systems a general proposal and a rhythmic case study, in: 2025 IEEE 64th Conference on Decision and Control, CDC, IEEE, 2025, pp. 962–967.
[19] Calvin Zhang, Timothy J. Lewis, Phase response properties of half-center oscillators, J. Comput. Neurosci. 35 (1) (2013) 55–74.
[20] Catherine Morris, Harold Lecar, Voltage oscillations in the barnacle giant muscle fiber, Biophys. J. 35 (1) (1981) 193–213.
[21] Arindam Basu, Paul E. Hasler, Nullcline-based design of a silicon neuron, IEEE Trans. Circuits Syst. I. Regul. Pap. 57 (11) (2010) 2938–2947.